

# Geophysical Research Letters<sup>®</sup>

## RESEARCH LETTER

10.1029/2021GL095699

### Key Points:

- A Tropical Cyclone (TC) inflow angle asymmetry model is developed to decompose synthetic aperture radar (SAR)-derived TC winds into rotation speeds and motion vector
- Validation against aircraft data shows the model-reconstructed wind speeds, and inflow angles are accurate even in areas not covered by SAR
- A systematic analysis of 130 SAR TC images using the model reveals that TC asymmetry and eye size decrease as TC intensity increases

### Correspondence to:

X. Li,  
[lix@qdio.ac.cn](mailto:lix@qdio.ac.cn)

### Citation:

Zhang, G., Li, X., Perrie, W., & Zhang, J. A. (2021). Tropical cyclone winds and inflow angle asymmetry from SAR imagery. *Geophysical Research Letters*, 48, e2021GL095699. <https://doi.org/10.1029/2021GL095699>

Received 17 AUG 2021

Accepted 6 OCT 2021

## Tropical Cyclone Winds and Inflow Angle Asymmetry From SAR Imagery

Guosheng Zhang<sup>1,2</sup>, Xiaofeng Li<sup>1</sup> , William Perrie<sup>2</sup> , and Jun A. Zhang<sup>3</sup> 

<sup>1</sup>Key Laboratory of Ocean Circulation and Waves, Institute of Oceanology, Chinese Academy of Sciences, Qingdao, China, <sup>2</sup>Fisheries and Oceans Canada, Bedford Institute of Oceanography, Dartmouth, NS, Canada, <sup>3</sup>National Oceanic and Atmospheric Administration/Atlantic Oceanographic and Meteorological Laboratory, Hurricane Research Division, University of Miami, Cooperative Institute for Marine and Atmospheric Studies, Miami, FL, USA

**Abstract** This study developed a morphological model for Tropical Cyclone (TC) wind and inflow angle asymmetry based on sea surface wind fields derived from spaceborne synthetic aperture radar (SAR) images. The model extracts the standard TC morphological information (center, intensity, and radius of the maximum wind) and decomposes the SAR-derived winds into vortex rotation winds and motion vector, making the reconstruction of the entire TC structure reliable, even in areas not mapped by SAR. The derived wind speeds and inflow angles are verified with aircraft measurements by stepped-frequency microwave radiometer and dropsondes, obtaining root-mean-square errors of 4.32 m/s and 16.04°, respectively. A systematic analysis of 130 SAR TCs images, collected by RADARSAT-2 and SENTINEL-1, reveals that the model can capture the main asymmetrical TC structure. Both TC asymmetry and eye size decrease as TC intensity increases.

**Plain Language Summary** Tropical Cyclone (TC) movement is essential in creating asymmetry in its surface winds. TCs include hurricanes and typhoons. However, the relations between asymmetrical TC surface wind field and TC movement are limited because of the lack of adequate observations. This study proposes an idealized model to investigate TC inflow angle asymmetry in the surface winds. The model has applied to 130 spaceborne synthetic aperture radar (SAR) images over a large variety of different TCs. This model can detect the asymmetrical surface wind structure, TC surface motion vectors and the associated inflow angles, and other standard morphological information such as center locations, symmetrical intensities, and radius of maximum winds. The model results are validated by comparing the wind speeds and inflow angles to measurements from the airborne stepped-frequency microwave radiometer and dropsondes, obtaining a root-mean-square error of 4.32 m/s and 16.04°, respectively. We compose TC surface wind speed distributions mapped by SAR and reconstructed by the model. They are shown to be similar in any TC category. The asymmetrical features are related to the storm intensity both in SAR winds and model results. In either the SAR observations or the model results, the maximum winds occur in the northeast quadrant.

## 1. Introduction

Tropical Cyclone (TC) studies aim to help the improvement of forecasts in order to protect human life and property from damage. TC wind plays a vital role in causing coastal damage incurred directly by the wind and indirectly due to ocean storm surges and surface waves, which pose a more significant threat to life and property than the winds. Storm surge models are mainly forced by surface winds, and the results are sensitive to wind errors (Lin & Chavas, 2012). Therefore, observations of the TC surface wind speed field, especially at a high spatial resolution, are important for society (Reul et al., 2017; B. Zhang & Perrie, 2012).

Since the first generation of meteorological satellites in the 1960s, cloud pictures acquired in passive remote sensing in the visible (Vis) and infrared (IR) bands have been applied to infer TC wind-related intensity and size estimations by using the Dvorak technique (Dvorak, 1975, 1984; Velden et al., 2006). Although the Dvorak method can successfully estimate TC intensity, the Vis and IR sensors cannot directly measure the surface winds. TC studies are often based on sea surface wind measurements by microwave instruments, such as Quick Scatterometer and Advanced Scatterometer (ASCAT) observations (Brennan et al., 2009; Klotz & Jiang, 2016, 2017), Soil Moisture and Ocean Salinity, and Soil Moisture Active Passive mission radiometer

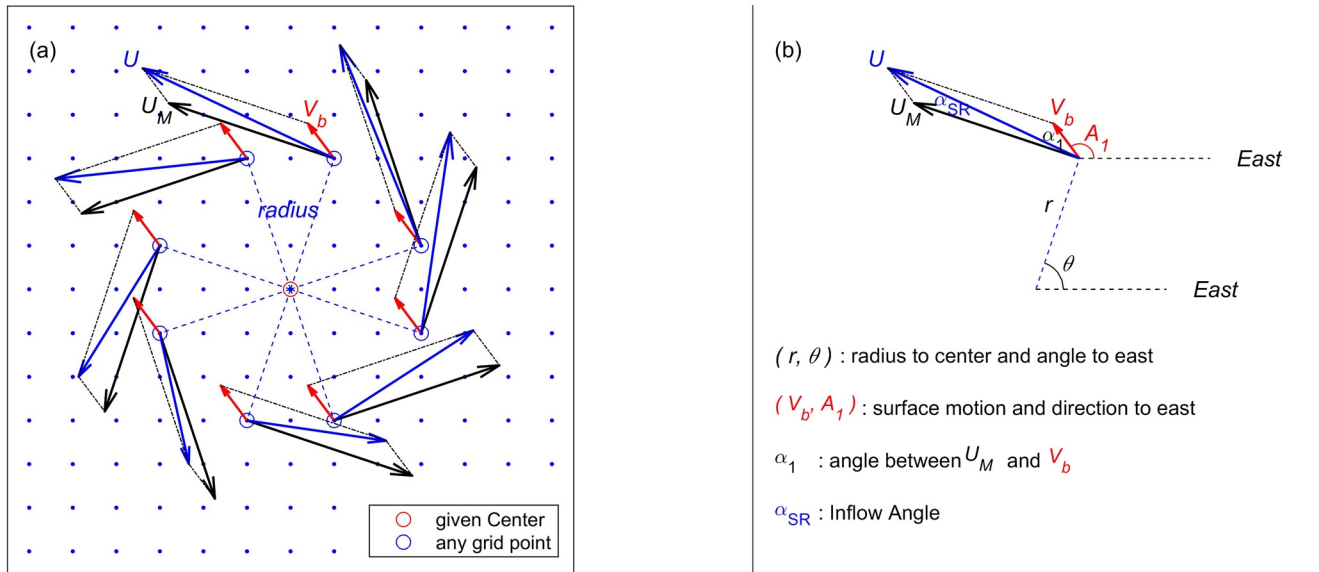


**Figure 1.** A schematic explanation of (a) wind simulation relative to a given center, (b) angles and vectors are for given points in the SHEW-2 model.

data (Reul et al., 2012, 2017). Compared to the abovementioned microwave instruments, synthetic aperture radar (SAR) has the advantage of high spatial resolution (tens of meters), allowing the monitoring and study of TC morphology and intensity (Li et al., 2013; G. Zhang & Perrie, 2018; Zhang et al., 2020).

Recently, an increasing number of SAR satellites have made many high-resolution images available for TC research. These include RADARSAT Constellation Mission, consisting of three identical satellites launched by Canada in 2019, Sentinel-1A and -1B by the European Space Agency (ESA) in 2014 and 2016, and ALOS-2 by Japan JAXA in 2014. Two issues still exist. First, SAR has a narrow swath often covering only parts of a given TC, creating a challenge to obtain the entire wind fields even with improved retrieval methods (Hwang et al., 2010, 2015; and Mouche et al., 2017, 2019), which are required for storm surge or surface wave modeling. Typically, the TC surface winds for storm surge or surface wave modeling are produced by an advanced numerical weather forecasting model (e.g., Colle et al., 2008) or reconstructed by parametric models (Emanuel et al., 2006; Lin et al., 2012; and Phadke et al., 2003). Second, as shown in high-resolution SAR-wind images, TCs are not symmetric vortex structures as assumed by earlier studies. TC movement is an essential factor in causing asymmetry in the surface winds. Zhang and Uhlhorn (2012) proposed a hurricane inflow angle model as a function of the storm forward motion based on dropwindsonde measurements from 187 aircraft flights. This study develops a new morphology model, SHEW-2 (Surface Hurricane Estimates for Wind speed and Wind direction) model, to understand Tropical Cyclone inflow angle asymmetry (TCIAA) imaged by SAR. We decompose the TC surface winds into the rotation winds of a symmetric vortex and a surface motion vector. We then apply the model to reconstruct the complete TC wind structure even in areas not covered by SAR.

Figure 1a shows a typical TC main structure. The sea surface wind field ( $\vec{U}$ ) is composed of the rotation wind ( $\vec{U}_m$ ) of an axisymmetric storm vortex and a surface motion vector ( $\vec{V}_b$ ) (Rego & Li, 2009; C. Zhang & Li, 2019). This study proposes a new reconstruction approach. We first derive the SAR surface wind using a known model, C-3PO, for C-band Cross-Polarization Coupled-Parameters Ocean (Zhang, Li, et al., 2017). We then decompose the winds into a surface motion vector ( $\vec{V}_b$ ) and the rotation wind ( $\vec{U}_m$ ) of a symmetric storm vortex. They can be combined to give the TCIAA surface wind structure.

The remainder of this letter is organized as follows. Section 2 presents the development of the TCIAA and its validation against airborne measurements from SFMR and dropwindsondes. Section 3 presents TCIAA model results for the analyses of TC asymmetrical structures from 130 SAR-derived wind images. Finally, conclusions are given in Section 4.

## 2. TCIAA Wind Model Based on SAR Observations

### 2.1. SHEW-2 Wind Model

In 2014, we proposed an original method (Zhang et al., 2014) to extract TC morphology from SAR-derived winds based on an axisymmetric model. In that version of the method, the TC center is detected from the original SAR image using a threshold methodology. In 2017, we modified the model by using an elliptical eye-wall vortex (Zhang, Perrie, et al., 2017). Thus, the TC center could be extracted from the SAR-derived wind field directly. This model was denoted “SHEW,” for Symmetric Hurricane Estimates for Wind. In 2020, we added “wavenumber-1” asymmetric structure to the SHEW model (Zhang et al., 2020).

Following the previous SHEW model, we denote the new morphology model for TCIAA as SHEW-2 to estimate surface wind vectors. The storm motion is supposed to be a major factor to induce the wavenumber-1 asymmetry (Klotz & Jiang, 2016, 2017). In other words, the TC asymmetry related to storm motion is part of the wavenumber-1 asymmetry. Therefore, the wavenumber-1 asymmetrical structure is not included in the SHEW-2 model. Therefore, the TCIAA surface wind vector is obtained by superimposing the surface motion vector onto the rotation wind of a symmetric TC vortex as:

$$\vec{U}(r, \theta) = (U \cdot \sin \alpha_{SR}, U \cdot \cos \alpha_{SR}) = \vec{U}_m(r) + \vec{V}_b \quad (1)$$

where  $U$  and  $\alpha_{SR}$  are the wind speed and TC sea surface inflow angle, respectively, from the SHEW-2 model. Here, we use  $\vec{U}_m(r)$  to represent the rotation wind vectors for the axisymmetric main flow, using the parameters  $U_{\max}$ ,  $r_m$ , and  $\alpha$ , which are based on the Rankine vortex function (Equation 2 in Zhang, Perrie, et al., 2017),  $\vec{V}_b$  is the surface motion vector, and  $(r, \theta)$  is the radius to the TC center and the angle to the east for each grid point. Here, the inflow angle ( $\alpha_{SR}$ ) is a function of the main vortex and the surface motion, defined as

$$\alpha_{SR}(\theta, r) = \tan^{-1} \frac{V_b \cdot \sin \alpha_1}{V_b \cdot \cos \alpha_1 + U_m(r)} \quad (2)$$

where  $V_b$  is the magnitude of the surface motion vector,  $U_m$  is the rotation wind speed of the main vortex, is the angle between the vectors  $\vec{U}_m(r)$ , and  $\vec{V}_b$ , defined as:

$$\alpha_1 = \frac{\pi}{2} + \theta - A_1 \quad (3)$$

where  $A_1$  is the surface motion vector direction to the east. Taking the SAR-derived winds as ground truth, we fit the reconstructed wind speed field ( $U$ ) to the sea surface wind retrieved from SAR using the least-squares method, where  $U$  is a function of the morphology parameters of ( $U_{\max}$ ,  $r_m$ ,  $\alpha$ ,  $V_b$ ,  $A_1$ ,  $lat_c$ , and  $long_c$ ). As a result, we can obtain the wind speeds ( $U$ ) of TCIAA, associated with the inflow angle ( $\alpha_{SR}$ ), as well as the morphology parameters ( $U_{\max}$ ,  $r_m$ ,  $\alpha$ ,  $V_b$ ,  $A_1$ ,  $lat_c$ , and  $long_c$ ).

A schematic explanation of the SHEW-2 model and a description of the angles and vectors in Equations 1–3 are displayed in Figures 1a and 1b, respectively. In this construction: (a) the radius ( $r$ ) is calculated with a given TC center, (b) the surface wind vector for the axisymmetric main vortex is computed by inputting the calculated radius ( $r$ ) associated with the parameters  $U_{\max}$ ,  $r_m$ , and  $\alpha$ , and (c)  $\vec{U}$  is combined with the surface motion vector ( $\vec{V}_b$ ) and the calculated main vortex ( $\vec{U}_m$ ).

Using Typhoon Bualoi (2019) as an example, we show the SAR-derived sea surface winds in Figure 2a and the results from the SHEW-2 model in Figures 2b and 2c, for example, best-fitted surface motion vectors ( $\vec{V}_b$ ) and rotation wind speeds ( $U_m$ ) as white vectors and color contours. The final SHEW-2 model results ( $\vec{U}$  and  $U$ ) are presented in Figure 2c. The extracted morphology parameters are:  $U_{\max} = 26.7$  m/s,  $r_m = 29.7$  km,  $\alpha = 0.8$ ,  $V_b = 5.1$  m/s,  $A_1 = 135^\circ$ , and the TC center at (12.36°N, 150.07°E).

### 2.2. Verifications

To validate the SHEW-2 model, we compare the estimated wind speeds to observations from the stepped-frequency microwave radiometers (SFMRs) onboard the National Oceanic and Atmospheric Administration WP-3D and U.S. Air Force aircraft. As shown in Figure 3, six cases were captured by both SAR and SFMR with time differences less than  $\pm 30$  min. The black lines show the SFMR flight tracks. The SFMR can

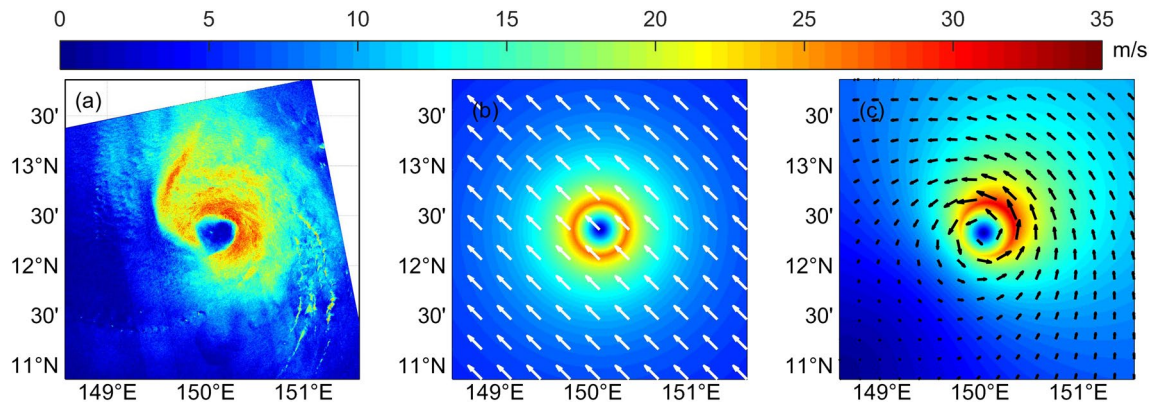


**Figure 2.** Example: (a) wind speeds derived from RADARSAT-2 ScanSAR image acquired at 15:02 UTC on October 20, 2019 over Typhoon Bualoi (2019), (b) extracted Tropical Cyclone surface motion (white vectors) and the axisymmetric main vortex (color), and (c) combined wind speed field.

provide along-track measurements of hurricane wind speeds by observing the wave breaking related brightness temperatures (Klotz & Uhlhorn, 2014; Uhlhorn & Black, 2003), at a spatial resolution of  $\sim 120$  m. Its temporal resolution is 1 Hz. Moreover, these SFMR winds are validated by dropwindsondes and in situ instrument measurements, with RMS errors of less than 4 and 5 m/s, respectively.

The resulting surface wind vectors ( $\vec{U}$ ) obtained by the SHEW-2 model are shown as arrows in Figure 3. The model results provide wind vectors outside SAR winds, which are also compared to the SFMR observations. We compare the SFMR measurements to the reconstructed surface winds from the rotation winds ( $U_m$ ) only and from the SHEW-2 model ( $U$ ) of TCIAA, in Figures 4a and 4b, respectively. There is a total of 14,208 collocated points. The bias between the SHEW-2 model (or rotation winds only) results and the SFMR measurements is 0.17 m/s (or  $-1.24$  m/s). Also the root mean square error (RMSE) is 4.32 m/s (or 5.71 m/s) and the correlation coefficient is 0.89 (or 0.81), respectively. This result demonstrates that the robustness of the SHEW-2 model, including the surface motion vector, is much better than that obtained by the rotation winds of symmetric vortex results. Using the SHEW models, we can also estimate the wind fields for areas outside the SAR observations.

We compare our results for the inflow angle to 22 dropwindsonde measurements acquired within  $\pm 30$  min of the satellite passes. The positions of these dropwindsonde measurements are shown as magenta crosses in Figure 3. As shown in Figure 4c, the bias is  $-12.00^\circ$ , the RMSE is  $16.04^\circ$ , and the correlation coefficient is 0.80. Unlike wind speed retrieval, the derivation of wind direction observations from remote sensing measurements is not straightforward. For example, the wind direction RMSE of the ASCAT onboard MetOp-A is about  $18^\circ$  (Bentamy et al., 2008).

Additionally, the TCs continue to move and rotate during the time differences between SAR and dropsonde measurements, contributing to the bias. The actual hurricane movements and rotations are hard to describe from the available data, leading to further complications in the verification process. The inflow angle features are also affected by subscale processes. By comparison, the inflow angle results from the SAR-observed wind speeds using the SHEW-2 model are determined from the surface motion vector.

### 3. TC Surface Wind Structure Revealed by TCIAA

We collected 130 RADARSAT-2, SENTINEL-1A, and -1B SAR TCs images in the northern hemisphere from 2016 to 2020 to characterize the TC asymmetry. Thus, we construct composite estimates for normalized wind speeds for different hurricane categories for the “actual” SAR-derived wind (right panels in Figure 5) and reconstructed winds from the TCIAA (SHEW-2) model (left panels in Figure 5). The TC intensities are indicated from the Saffir-Simpson hurricane wind scale and the number of cases observed by SAR. There are: (a) 40 cases for TCs weaker than category 1 hurricane (H0) with  $u_{\max} < 64$  kt (1 kt = 0.5144 m/s), (b) 37 cases of category 1 hurricane (H1) with  $64 \text{ kt} \leq u_{\max} < 83$  kt, (c) 30 cases of categories 2 and 3 hurricanes (H23) with  $83 \text{ kt} \leq u_{\max} < 113$  kt, and (d) 23 cases of categories 4 and 5 hurricanes (H45) with  $u_{\max} \geq 113$  kt.



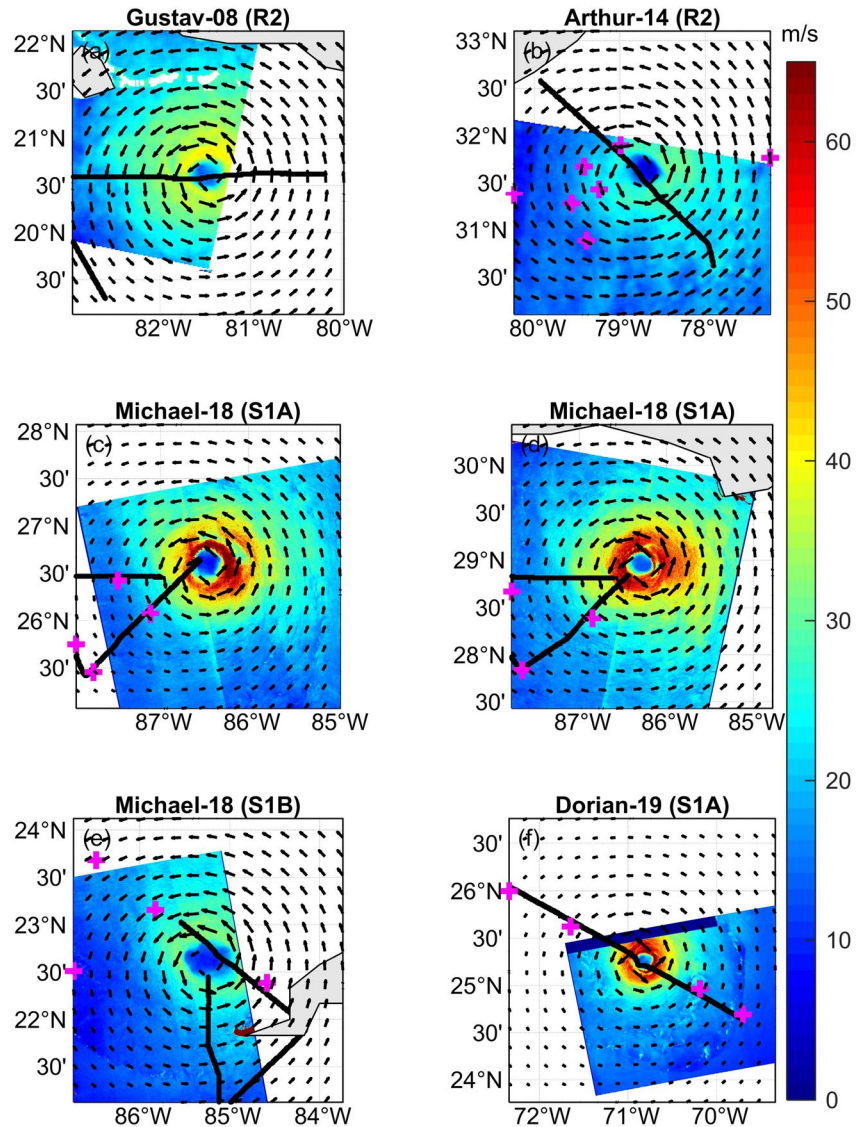


**Figure 3.** SAR-derived sea surface winds (colors), model results (arrows) and the associated aircraft flight tracks (lines), and the positions of the dropwindsondes (crosses) within  $\pm 30$  min: (a) from RADARSAT-2 acquired at 11:28 UTC of August 30, 2008, (b) from RADARSAT-2 acquired at 11:13 UTC of July 03, 2014, (c) from SENTINEL-1A acquired at 23:45 UTC on October 9, 2018, (d) from Sentinel-1A acquired at 11:50 UTC on October 10, 2018, (e) from Sentinel-1B acquired at 23:51 UTC on October 8, 2018, and (f) from Sentinel-1A acquired at 22:46 UTC on August 30, 2019.

The left panels present the surface wind ( $u_{10}$ ) reconstructions using the SHEW-2 model, indicating asymmetrical storm structures related to TC motions. The right panels present SAR-derived  $u_{10}$  and represent the “actual” surface winds. The normalized wind speeds are computed as  $u_{10}/u_{\max}$ , and the normalized distance is calculated as  $r/r_m$ , where  $r$  is the radius and  $r_m$  is the radius of maximum wind (RMW). The hurricane center, RMW, and  $u_{\max}$  are all from the SHEW-2 model. Thus, the normalized wind speeds can be larger than 1 due to the effects of asymmetries. Each sub-image in Figure 5 is derived by the average of all TCs in that category.

To describe the asymmetric structures, we estimate the center of the wind speed ( $x_R, y_R$ ) as:

$$(x_R, y_R) = \left( \sum_{i=1}^n u_i x_i / \sum_{i=1}^n u_i, \sum_{i=1}^n u_i y_i / \sum_{i=1}^n u_i \right) \quad (4)$$

where  $(x_i, y_i)$  are normalized Cartesian coordinates and  $u_i$  is the normalized wind speed. The calculated positions are shown as white crosses in Figure 5. All the calculated centers are in the northeast quadrants. For

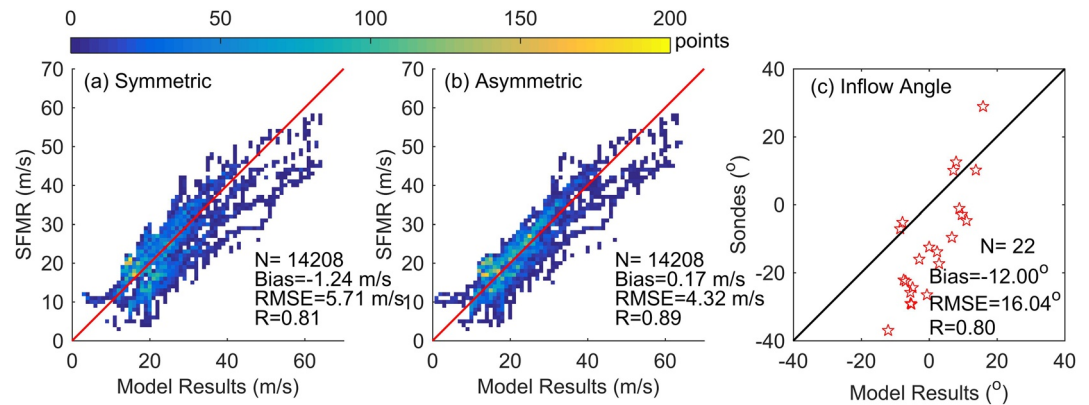


**Figure 4.** Verifications comparing: (a) SFMR measurements to the (old) SHEW model results with only symmetrical main vortex, (b) same as (a) but for SHEW-2 model results, and (c) inflow angles from SHEW-2 model results to dropsonde measurements.

the SHEW-2 model results (Figure 5, left panels), the normalized radii of the wind speed centers are 0.283, 0.150, 0.0864, and 0.200 for the TC 4 categories. For actual SAR winds (Figure 5, right panels), the distances are 0.307, 0.198, 0.159, and 0.237, respectively.

The right panels are the entire wind fields of hurricanes containing various asymmetries imaged by SAR. Although the TCIAA is extracted from the SAR retrievals, no asymmetry except the TCIAA is included in the left panels. If the total other asymmetric features in the SAR retrievals surpass the TCIAA, the left and right panels would be different from each other. For a given hurricane category, the wind structure from the SHEW-2 model (left panels) is similar to the “actual” surface wind structure (right panels), demonstrating that the extracted TCIAA values carry most of the SAR-derived “actual” wind features. In other words, the main TC structure mapped by SAR is the TCIAA structure. Second, the asymmetry features decline with increasing storm intensity, consistent with previous results based on satellite observations (Klotz & Jiang 2016, 2017). This difference may be associated with convective asymmetry in TCs with different intensities and intensity change rates. Previous studies found that intensifying storms have more symmetric distributions due to deep convection than steady-state storms, which is partly tied to the environmental shear difference and boundary layer processes (e.g., Rogers et al., 2016; J. A. Zhang & Rogers, 2019). Our results support the view that stronger storms tend to have more symmetric distributions for the surface winds. Third, the estimated centers of the wind speed ( $x_R$ ,  $y_R$ ) occur in the northeast quadrant, with azimuth angles of 59.18°, 55.06°, 44.72°, and 57.72° to the east for the model results, and 73.99°, 47.19°, 65.39°, and 70.89° for SAR-derived wind fields, for the four TC categories, respectively. Finally, surface wind fields in TCs become more spatially concentrated as the intensities increase. The averaged RMWs for the four categories are 36.26, 35.60, 32.45, and 18.99 km, which means the TC eye size decreases as the intensity increases.

#### 4. Conclusions

A SHEW-2 model is proposed to detect TCIAA wind structure and associated parameters from SAR-derived surface wind speeds. We apply this SHEW-2 model to 130 SAR-derived sea surface wind fields, with high spatial resolution ( $\sim 1$  km), collected over TCs by RADARSAT-2, SENTINEL-1A, and SENTINEL-1B. Thus, we detect the TCIAA surface wind structures, TC surface motion vectors, associated inflow angles, and morphological information such as the center locations, symmetrical intensities, and RMWs. The TC wind structure provided by the SHEW-2 model is complete and tends to be larger than that observed by the SAR image.

Compared to the SFMR measurements, the model estimates for wind speeds in the SAR coverage area have RMSE of 4.32 m/s and a correlation coefficient of 0.89. The detected TC sea surface inflow angles are verified with dropsonde measurements, with RMSE of 16.04° and acceptable correlation coefficients at about 0.80. Since the SHEW-2 model only relates TC sea surface inflow angles to the asymmetrical mean structure (or surface motion vector), we provide an error analysis to estimate possible limiting considerations: (a)

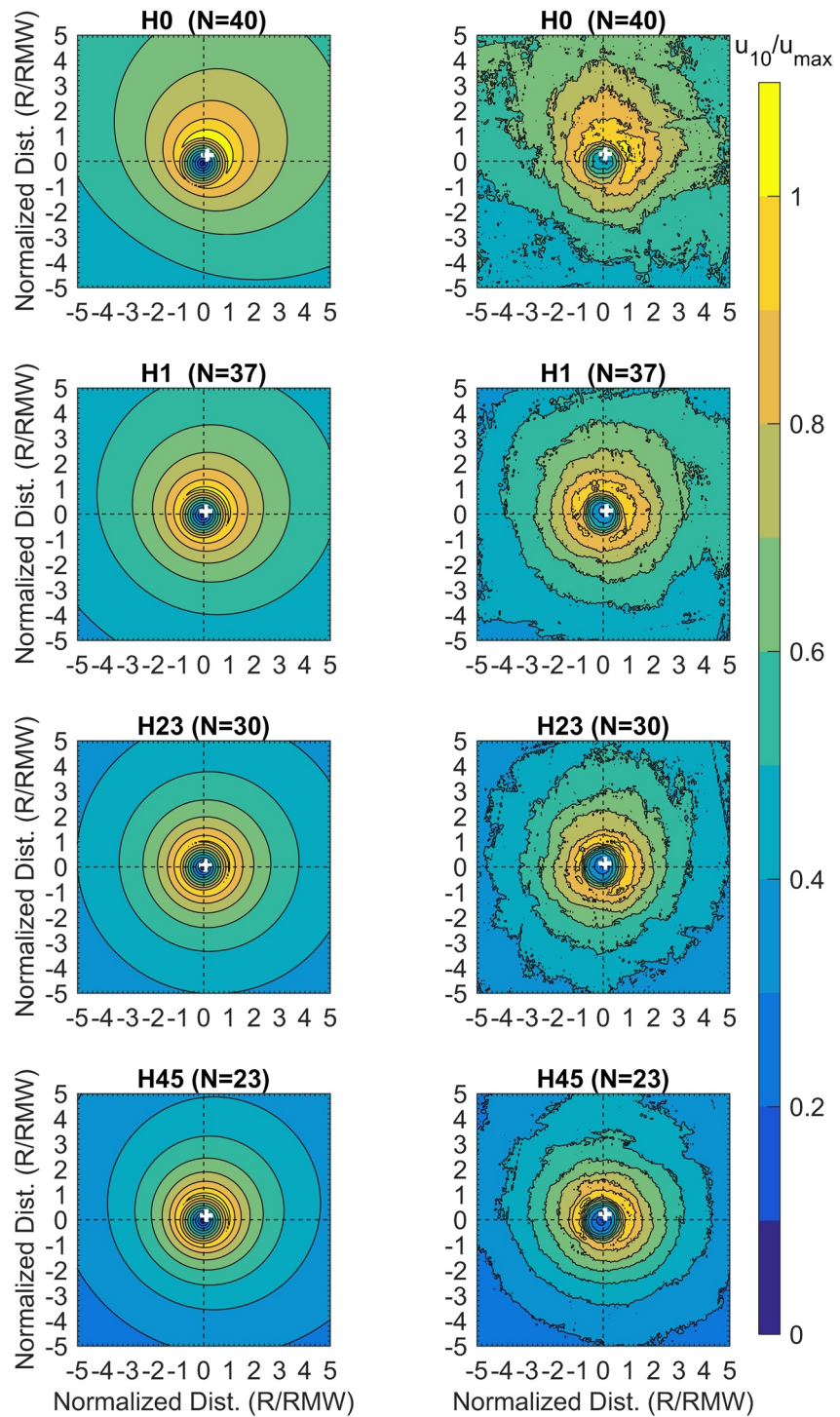


**Figure 5.** Composite normalized wind speed analyses for different intensities (H0, H1, H23, and H45) for SHEW-2 model results (left panels) and from actual SAR-derived wind (right panels). Storm-centered figures are plotted using the detected RMW ( $r_m$ ) and hurricane centers, using a normalized distance,  $r/r_m$ . Counter lines are plotted in increments of 0.1 normalized units ( $u_{10}/u_{\max}$ ). Each sub-image in the figure is derived by the average of all TCs in that category.



difficulties in wind direction retrievals, (b) time differences between SAR and dropsonde data, and (c) TC internal subscale processes. The TC inflow angle model (Equations 2 and 3) proposed here can also be used without SAR observations. Using the motion vector from Best Track data ( $\vec{V}_b = 0.5 \cdot \vec{V}_{BT}$ ) (Lin et al., 2012), then  $U_m$  can be computed by the Rankine vortex function (Equation 2, Zhang, Perrie, et al., 2017) or by a function like  $U_m(r) = 2 u_{\max} r/r_m/[1 + (r/r_m)^2]$ , and the TC sea surface inflow angle can be simulated.

A composite analysis is carried out. The results show that the composite SAR-derived wind structures are similar to those from model results, demonstrating that SHEW-2 can provide the main asymmetrical structures imaged by SAR. In both model results and SAR observations, all estimated TC centers ( $x_R, y_R$ ) are located in the northeast quadrant. Using the model, a systematic analysis of 130 SAR TC images reveals TC asymmetry and eye size decreases as TC intensity increases.

As the wind field derived from SAR is at the sea surface level (referenced to 10 m height), the motion vector extracted by the SHEW-2 model is also at the sea surface level. Because adequate observations are limited, the relationship between the motions at the surface and free-troposphere height is still a research topic (e.g., Emanuel et al., 2006; Lin et al., 2012; Phadke et al., 2003). Generally, the TC's movement is mainly due to advection by the background wind surrounding the TC vortex. The storm motion speed is thus supposed to be an averaged environmental flow of the whole troposphere. However, the surface motion can deviate from that of the free troposphere above the boundary layer, due to surface friction. Therefore, the error and uncertainty in the diagnosed storm motion from SAR by the SHEW-2 model are complicated and can be affected by TC motion in free-troposphere height, by surface friction, by the large-scale environmental vertical wind shear, and related factors.

## Data Availability Statement

The RADARSAT-2 data were provided by the Canadian Space Agency under the Hurricane Watch project, which can be acquired from Earth Observation Data Management System (<https://www.eodms-sgdot.nrcan-rncan.gc.ca>). The Sentinel-1 data were provided by the European Space Agency (<https://eoda.cls.fr/client/oceano/#Sentinel>). The SFMR and dropsonde data were provided by NOAA ([https://www.aoml.noaa.gov/hrd/data\\_sub/hurr.html](https://www.aoml.noaa.gov/hrd/data_sub/hurr.html)).

## Acknowledgments

The work was supported by the Strategic Priority Research Program of the Chinese Academy of Sciences (CAS) (XDB42040401), the National Key Research and Development Program of China (2019YFC1510100), the Innovation Group Project of Southern Marine Science and Engineering Guangdong Laboratory (Zhuhai) (311020004), the Open Foundation from Marine Sciences in the First-Class Subjects of Zhejiang (20200102), the Startup Foundation for Introducing Talent of NUIST, the Key R & D project of Shandong Province (2019JZZY010102), the Key deployment project of Center for Ocean Mega-Science, CAS (COMS2019R02), and the CAS (Y9KY04101L).

## References

- Bentamy, A., Croize-Fillon, D., & Perigaud, C. (2008). Characterization of ASCAT measurements based on buoy and QuikSCAT wind vector observations. *Ocean Science*, 4(4), 265–274. <https://doi.org/10.5194/os-4-265-2008>
- Brennan, M. J., Hennon, C. C., & Knabb, R. D. (2009). The operational use of QuikSCAT ocean surface vector winds at the National Hurricane Center. *Weather and Forecasting*, 24(3), 621–645. <https://doi.org/10.1175/2008WAF2222188.1>
- Colle, B. A., Buonaiuto, F., Bowman, M. J., Wilson, R. E., Flood, R., Hunter, R., & Hill, D. (2008). New York City's vulnerability to coastal flooding: Storm surge modeling of past cyclones. *Bulletin of the American Meteorological Society*, 89(6), 829–842. <https://doi.org/10.1175/2007BAMS2401.1>
- Dvorak, V. F. (1975). Tropical cyclone intensity analysis and forecasting from satellite imagery. *Monthly Weather Review*, 103(5), 420–430. [https://doi.org/10.1175/1520-0493\(1975\)103<0420:TCIAAF>2.0.CO;2](https://doi.org/10.1175/1520-0493(1975)103<0420:TCIAAF>2.0.CO;2)
- Dvorak, V. F. (1984). Tropical Cyclone Intensity Analysis Using Satellite Data (Vol. 11). US Department of Commerce, National Oceanic and Atmospheric Administration, National Environmental Satellite, Data, and Information Service.
- Emanuel, K., Ravela, S., Vivant, E., & Risi, C. (2006). A statistical deterministic approach to hurricane risk assessment. *Bulletin of the American Meteorological Society*, 87(3), 299–314. <https://doi.org/10.1175/BAMS-87-3-299>
- Hwang, P. A., Stoffelen, A., van Zadelhoff, G. J., Perrie, W., Zhang, B., Li, H., & Shen, H. (2015). Cross-polarization geophysical model function for C-band radar backscattering from the ocean surface and wind speed retrieval. *Journal of Geophysical Research: Oceans*, 120(2), 893–909. <https://doi.org/10.1002/2014JC010439>
- Hwang, P. A., Zhang, B., & Perrie, W. (2010). Depolarized radar return for breaking wave measurement and hurricane wind retrieval. *Geophysical Research Letters*, 37(1), L01604. <https://doi.org/10.1029/2009GL041780>
- Klotz, B. W., & Jiang, H. (2016). Global composites of surface wind speeds in tropical cyclones based on a 12 year scatterometer database. *Geophysical Research Letters*, 43(19), 10480–10488. <https://doi.org/10.1002/2016GL071066>
- Klotz, B. W., & Jiang, H. (2017). Examination of surface wind asymmetries in tropical cyclones. Part I: General structure and wind shear impacts. *Monthly Weather Review*, 145(10), 3989–4009. <https://doi.org/10.1175/MWR-D-17-0019.1>
- Klotz, B. W., & Uhlhorn, E. W. (2014). Improved stepped frequency microwave radiometer tropical cyclone surface winds in heavy precipitation. *Journal of Atmospheric and Oceanic Technology*, 31(11), 2392–2408. <https://doi.org/10.1175/JTECH-D-14-00028.1>
- Li, X., Zhang, J. A., Yang, X., Pichel, W. G., DeMaria, M., Long, D., & Li, Z. (2013). Tropical cyclone morphology from spaceborne synthetic aperture radar. *Bulletin of the American Meteorological Society*, 94(2), 215–230. <https://doi.org/10.1175/BAMS-D-11-00211.1>
- Lin, N., & Chavas, D. (2012). On hurricane parametric wind and applications in storm surge modeling. *Journal of Geophysical Research*, 117(D9), D09120. <https://doi.org/10.1029/2011JD017126>



- Lin, N., Emanuel, K., Oppenheimer, M., & Vanmarcke, E. (2012). Physically based assessment of hurricane surge threat under climate change. *Nature Climate Change*, 2(6), 462–467. <https://doi.org/10.1038/nclimate1389>
- Mouche, A., Chapron, B., Knaff, J., Zhao, Y., Zhang, B., & Combot, C. (2019). Copolarized and cross-polarized SAR measurements for high-resolution description of major hurricane wind structures: Application to Irma category 5 hurricane. *Journal of Geophysical Research: Oceans*, 124(6), 3905–3922. <https://doi.org/10.1029/2019JC015056>
- Mouche, A. A., Chapron, B., Zhang, B., & Husson, R. (2017). Combined co-and cross-polarized SAR measurements under extreme wind conditions. *IEEE Transactions on Geoscience and Remote Sensing*, 55(12), 6746–6755. <https://doi.org/10.1109/TGRS.2017.2732508>
- Phadke, A. C., Martino, C. D., Cheung, K. F., & Houston, S. H. (2003). Modeling of tropical cyclone winds and waves for emergency management. *Ocean Engineering*, 30(4), 553–578. [https://doi.org/10.1016/S0029-8018\(02\)00033-1](https://doi.org/10.1016/S0029-8018(02)00033-1)
- Rego, J. L., & Li, C. (2009). On the importance of the forward speed of hurricanes in storm surge forecasting: A numerical study. *Geophysical Research Letters*, 36(7), L07609. <https://doi.org/10.1029/2008GL036953>
- Reul, N., Chapron, B., Zabolotskikh, E., Donlon, C., Mouche, A., Tenerelli, J., et al. (2017). A new generation of tropical cyclone size measurements from space. *Bulletin of the American Meteorological Society*, 98(11), 2367–2385. <https://doi.org/10.1175/BAMS-D-15-00291.1>
- Reul, N., Tenerelli, J., Chapron, B., Vandemark, D., Quilfen, Y., & Kerr, Y. (2012). SMOS satellite L-band radiometer: A new capability for ocean surface remote sensing in hurricanes. *Journal of Geophysical Research*, 117(C2), C02006. <https://doi.org/10.1029/2011JC007474>
- Rogers, R. F., Zhang, J. A., Zawislak, J., Jiang, H., Alvey, G. R., III, Zipser, E. J., & Stevenson, S. N. (2016). Observations of the structure and evolution of Hurricane Edouard (2014) during intensity change. Part II: Kinematic structure and the distribution of deep convection. *Monthly Weather Review*, 144(9), 3355–3376. <https://doi.org/10.1175/MWR-D-16-0017.1>
- Uhlhorn, E. W., & Black, P. G. (2003). Verification of remotely sensed sea surface winds in hurricanes. *Journal of Atmospheric and Oceanic Technology*, 20(1), 99–116. [https://doi.org/10.1175/1520-0426\(2003\)020<0099:VORSSS>2.0.CO;2](https://doi.org/10.1175/1520-0426(2003)020<0099:VORSSS>2.0.CO;2)
- Velden, C., Harper, B., Wells, F., Beven, J. L., Zehr, R., Olander, T., et al. (2006). The Dvorak tropical cyclone intensity estimation technique: A satellite-based method that has endured for over 30 years. *Bulletin of the American Meteorological Society*, 87(9), 1195–1210. <https://doi.org/10.1175/BAMS-87-9-1195>
- Zhang, B., & Perrie, W. (2012). Cross-polarized synthetic aperture radar: A new potential measurement technique for hurricanes. *Bulletin of the American Meteorological Society*, 93(4), 531–541. <https://doi.org/10.1175/BAMS-D-11-00001.1>
- Zhang, C., & Li, C. (2019). Effects of hurricane forward speed and approach angle on storm surges: An idealized numerical experiment. *Acta Oceanologica Sinica*, 38(7), 48–56. <https://doi.org/10.1007/s13131-018-1081-z>
- Zhang, G., Li, X., Perrie, W., Hwang, P. A., Zhang, B., & Yang, X. (2017). A hurricane wind speed retrieval model for C-band RADARSAT-2 cross-polarization ScanSAR images. *IEEE Transactions on Geoscience and Remote Sensing*, 55(8), 4766–4774. <https://doi.org/10.1109/TGRS.2017.2699622>
- Zhang, G., & Perrie, W. (2018). Effects of asymmetric secondary eyewall on tropical cyclone evolution in Hurricane Ike (2008). *Geophysical Research Letters*, 45(3), 1676–1683. <https://doi.org/10.1002/2017GL076988>
- Zhang, G., Perrie, W., Li, X., & Zhang, J. A. (2017). A hurricane morphology and sea surface wind vector estimation model based on C-band cross-polarization SAR imagery. *IEEE Transactions on Geoscience and Remote Sensing*, 55(3), 1743–1751. <https://doi.org/10.1109/TGRS.2016.2631663>
- Zhang, G., Perrie, W., Zhang, B., Yang, J., & He, Y. (2020). Monitoring of tropical cyclone structures in ten years of RADARSAT-2 SAR images. *Remote Sensing of Environment*, 236, 111449. <https://doi.org/10.1016/j.rse.2019.111449>
- Zhang, G., Zhang, B., Perrie, W., Xu, Q., & He, Y. (2014). A hurricane tangential wind profile estimation method for C-band cross-polarization SAR. *IEEE Transactions on Geoscience and Remote Sensing*, 52(11), 7186–7194. <https://doi.org/10.1109/TGRS.2014.2308839>
- Zhang, J. A., & Rogers, R. F. (2019). Effects of parameterized boundary layer structure on hurricane rapid intensification in shear. *Monthly Weather Review*, 147(3), 853–871. <https://doi.org/10.1175/MWR-D-18-0010.1>
- Zhang, J. A., & Uhlhorn, E. W. (2012). Hurricane sea surface inflow angle and an observation-based parametric model. *Monthly Weather Review*, 140(11), 3587–3605. <https://doi.org/10.1175/MWR-D-11-00339.1>